Gao, Weiyin; Ran, Chenxin; Li, Jingrui; Dong, Hua; Jiao, Bo; Zhang, Lijun; Lan, Xuguang; Hou, Xun; Wu, Zhaoxin

Robust Stability of Efficient Lead-Free Formamidinium Tin Iodide Perovskite Solar Cells Realized by Structural Regulation

Published in:
Journal of Physical Chemistry Letters

DOI:
10.1021/acs.jpclett.8b03194

Published: 20/12/2018

Document Version
Peer reviewed version

Please cite the original version:
Gao, W., Ran, C., Li, J., Dong, H., Jiao, B., Zhang, L., Lan, X., Hou, X., & Wu, Z. (2018). Robust Stability of Efficient Lead-Free Formamidinium Tin Iodide Perovskite Solar Cells Realized by Structural Regulation. *Journal of Physical Chemistry Letters*, *9*(24), 6999-7006. https://doi.org/10.1021/acs.jpclett.8b03194

DOI: 10.1021/acs.jpclett.8b03194

Robust Stability of Efficient Lead-Free Formamidinium Tin Iodide Perovskite Solar Cells Realized by Structural Regulation

Weiyin Gao [a], Chenxin Ran [a], Jingrui Li [b], Hua Dong [a], Bo Jiao [a], Lijun Zhang [c], Xuguang Lan [d], Xun Hou [a], and Zhaoxin Wu [*,a]

[a] Key Laboratory of Photonics Technology for Information, Key Laboratory for Physical Electronics and Devices of the Ministry of Education, School of Electronic and Information Engineering, Xi'an Jiaotong University, Xi'an 710049, P.R. China

[b] Department of Applied Physics, Aalto University, FI-00076 AALTO, Finland

[c] State Key Laboratory of Superhard Materials, Key Laboratory of Automobile Materials of MOE, and College of Materials Science and Engineering, Jilin University, Changchun 130012, China

[d] Institute of Artificial Intelligence and Robotics, Xi'an Jiaotong University, Xi'an 710049, China

[e] Collaborative Innovation Center of Extreme Optics, Shanxi University, Taiyuan 030006, China

*Corresponding author. E-mail: zhaoxinwu@mail.xjtu.edu.cn

ABSTRACT

The instability issue of Pb-free Sn-based perovskite is one of the biggest challenges for its application in optoelectronic devices. Herein, a structural regulation strategy is demonstrated to regulate the geometric symmetry of formamidiniumtin iodide ($FASnI_3$) perovskite. Experimental and theoretical works show that the introduction of cesium cation (Cs^+) could improve the geometric symmetry, suppress the oxidation of Sn^{2+}, and enhance the thermodynamical structural stability of $FASnI_3$. As a result, the inverted planar Cs-doped $FASnI_3$-based perovskite solar cell (PSC) is shown to maintain 90% of its initial power-conversion efficiency (PCE) after 2000 h stored in N_2, which is the best durability to date for 3D Sn-based PSCs. Most importantly, the air, thermal, and illumination stabilities of the PSCs are all improved after Cs doping. The PCE of the Cs-doped PSC shows a 63% increase compared to that of the control device (from 3.74% to 6.08%) due to the improved quality of the Cs-doped $FASnI_3$ film.

Organic-inorganic hybrid lead halide perovskite material has made great progress in the field of optoelectronic applications [1−3]. After a few years of development, the power conversion efficiency (PCE) of solar cells based on organic-inorganic lead halide perovskite materials has been rapidly improved to as high as 23.3% [4−6]. The toxicity problem of this material, however, is still one of the biggest challenges that limits its practical large-scale commercialization. With this in mind, research efforts have been dedicated to developing other perovskite materials with lead-free metals for photovoltaic application [7]. To date, the photovoltaic performance of devices with alternatives to Pb, including Sn [8], Ge [9]. Bi [10,11], Sb [12], and Cu [13], is still much lower than their Pb-based references. Among all these alternatives, Sn-based perovskite materials are the most promising because of the two valence electrons of Sn^{2+} for maintaining the 3D structure, suitable band gap for sunlight harvesting, and high carrier mobility [14]. Recently, perovskite solar cells (PSCs) based on formamidinium tin iodide ($FASnI_3$) perovskite material have made significant progress, and the PCE of the device is approaching 9% [15−27].

For $FASnI_3$-based PSCs, the instability issue is still an urgent problem that needs to be solved. Although theoretical study has found that the Sn atom in $FASnI_3$ is less likely to be oxidized than in $MASnI_3$ because of the stronger hydrogen bond in $FASnI_3$ [28], it is generally agreed that the oxidation of Sn^{2+} into Sn^{4+} is the main reason for device malfunction of the $FASnI_3$-based PSCs. Because tin is in the middle of group 14 in the periodic table, both 2+ and 4+ oxidation states are equally thermodynamically stable [8]. As a result, coexistence of Sn^{2+} and Sn^{4+} in Sn-based perovskite can be expected. This coexistence of Sn^{2+} and Sn^{4+} is also observed in $CuZnSnS_4$ material, even though Sn^{4+} is the main oxidation state [29]. It is also observed that when no reducing agent is present, the oxidation of Sn^{2+} into Sn^{4+} can be a spontaneous process [15]. To enhance the stability of Sn-based perovskite, many effective strategies have been developed, such as Sn compensation [30−32], reduction additive [33] or atmosphere [34], and structural dimension reduction [20,26,27]. In addition to the easy oxidation of Sn^{2+}, the crystal-structure analysis of $FASnI_3$ indicates that its structure deviates from an ideal perovskite and might cause the instability of the material. The geometrical configuration of the ABX_3 perovskite material can be described by the Goldschmidt tolerance factor t [35]

$$t = \frac{R_A + R_B}{\sqrt{2}(R_B + R_X)}$$

where R_A, R_B, and R_X are the ionic radii of A, B, and X ions, respectively. For an ideal symmetrical cubic ABX_3 perovskite structure with high structural stability, the tolerance factor should be close to 1. In the case of $FASnI_3$, t is calculated to be 1.04 (R_{FA^+} = 253 pm, $R_{Sn^{2+}}$ = 102 pm, R_{I^-} = 220 pm) [36,37], which is a little greater than 1, indicating the expansion tendency of SnI_6 octahedral caused by FA^+ with larger ion size in the crystal structure. Therefore, doping A site ion by ions with smaller ionic radius, which could contract the crystal lattice of $FASnI_3$, should be a rational strategy to improve the structural stability of $FASnI_3$ perovskite. However, little attention has been paid to the crucial role of this structural regulation strategy on the stability and photovoltaic performance of $FASnI_3$ perovskite to date, and it is desired to develop effective strategies to investigate this issue.

In this work, a structural regulation strategy is proposed, which is realized by the introduction of Cs into the structural lattice of $FASnI_3$. It should be noted that the t value of $MASnI_3$ is 0.88 (R_{MA^+} = 180 pm) [38], and doping of Cs could only further destroy the symmetry of the structure. Therefore, here we focus on only the structural regulation of $FASnI_3$. The doping effect of Cs on the features of $FASnI_3$ structure is systematically investigated both theoretically and experimentally. Cs is shown to insert into the lattice of $FASnI_3$ structure and induce the contraction of the corner-sharing SnI_6 octahedra, which improves the geometric symmetry of the $FASnI_3$ structure. Also, the oxidation of Sn^{2+} is significantly suppressed after Cs-doping. Theoretical calculation results demonstrate the reduced free energy and improved structure symmetry of $FASnI_3$ after Cs doping, which leads to its energetically superior stability. Moreover, the quality of $FASnI_3$ film (grain size, crystallinity, trap state density, and light response range) is found to be improved after Cs doping, and the PSCs based on this Cs-doping film achieves PCE as high as 6.08% with negligible hysteresis and improved device reproducibility. Most importantly, the PSC device after Cs doping retains 90% of its initial PCE after storage in N_2 for 2000 h and also exhibits significantly improved device stability against air, heat, and illumination.

To study the role of Cs doping on the characteristics of $FASnI_3$ film, we fabricate the $Cs_xFA_{1-x}SnI_3$ films using antisolvent rapid crystallization technology (for details, see Experimental Section in the Supporting Information) [39]. The doping of Cs is realized by the addition of a given amount of CsI in the precursor. Figure 1a−e shows the SEM images of $Cs_xFA_{1-x}SnI_3$ films; it can be found that all the films show the surface morphology of densely packed grains, which is a benefit of the antisolvent rapid crystallization technology used. Also, the root-mean-square (RMS) roughness of these films is ~10 nm (Figure S1), demonstrating the smoothness of these films. When the Cs doping content is less than 20%, an increased grain size of the film can be observed, as shown in the statistical distribution of grain size (Figure 1f). This enlarged crystal size is well-correlated with the XRD pattern, where the intensity of the diffraction peak increases after Cs doping. Figure 1g shows the XRD pattern of $Cs_xFA_{1-x}SnI_3$ films, and the diffraction peaks match the crystallized orthorhombic $FASnI_3$ crystal in an Amm2 space group with random orientation [17]. However, further increasing the Cs content leads to decreased grain size (≥40%), which is due to the dominant $CsSnI_3$ phase with small grain size when Cs content is high (Figure S2). This can be also evidenced by the XRD pattern in which typical diffraction peaks of $CsSnI_3$ become dominant when Cs content is greater than 40% (Figure 1g). In addition, the XRD peak position exhibits an obvious shift toward higher degree (Figure 1h), indicating the successful incorporation of Cs into the crystal lattice of $FASnI_3$. Besides, the shift toward higher degree also suggests the shrinkage of the crystal lattice, which indicates the contraction tendency of $FASnI_3$ structure after Cs doping. Ultraviolet− visible (UV−vis) spectra of the $Cs_xFA_{1-x}SnI_3$ films (Figure 1i) show that the absorption intensity is enhanced in the range of 500−900 nm upon the Cs doping, and the absorption edge is red-shifted, which agrees with the red-shifted PL spectra of the $Cs_xFA_{1-x}SnI_3$ films (Figure 1j). This red-shift tendency of Sn perovskite after Cs doping is opposite to the blue-shift in Pb perovskite after Cs doping. This difference is proposed to be due to the different structural evolutions of Sn and Pb perovskite after Cs doping. For $FASnI_3$, the crystal lattice will contract from expanded octahedral ($FASnI_3$, t = 1.04) to cubic structure ($Cs_xFA_{1-x}SnI_3$, $t \approx 1$), and this contraction could destabilize the valence band (VB) of $FASnI_3$ and raises its energy level of VB, resulting in the band gap reduction [40]. For $FAPbI_3$, the crystal lattice will tilt from cubic structure ($FAPbI_3$, t = 0.99) to distorted octahedral ($Cs_xFA_{1-x}PbI_3$, t < 0.90), and this tetragonal distortion originates from a reduction of the metal-halide-metal bond angle below the value of 180°, leading to the reduced overlap between metal and halide orbitals as well as lowered VB [40].

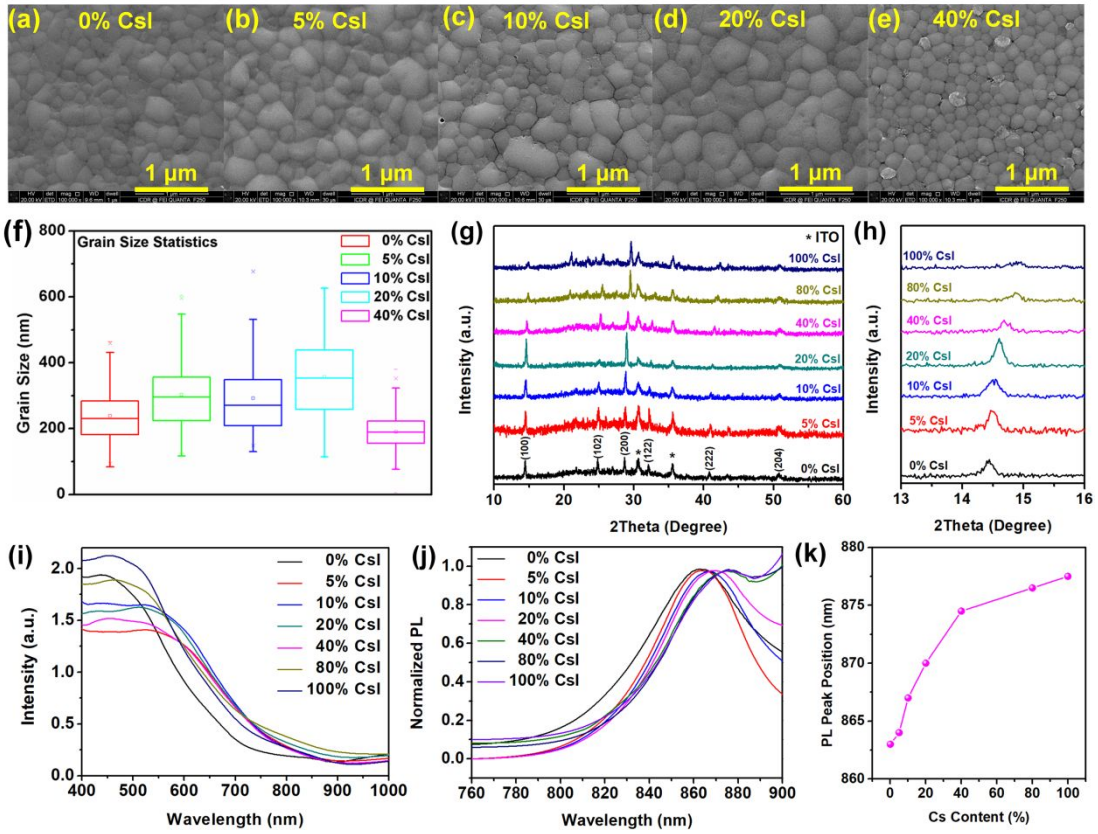

Figure 1. (a−e) SEM images, (f) grain size statistics, (g and h) XRD patterns, (i) UV−vis spectra, (j) PL spectra, and (k) PL peak position variation of $Cs_xFA_{1-x}PbI_3$ films.

Next, to study the photovoltaic performance of the $Cs_xFA_{1-x}SnI_3$ films, we fabricate PSCs with inverted device structure of ITO/PEDOT:PSS/$Cs_xFA_{1-x}SnI_3$/C60/BCP/Ag (Figure 2a). The thickness of the $Cs_xFA_{1-x}SnI_3$ layer is measured to be ~200 nm (Figure 2b). To set a control PSCs device, we first systematically optimize the film fabrication parameters of $FASnI_3$ film, including precursor concentration (Figure S3), solvent composition (Figure S4), and annealing temperature (Figure S5). The detailed film fabrication process is provided in the Supporting Information. Then we investigate the effect of Cs doping on the photovoltaic performance of PSCs (Figure 2c). Table 1 collects the *J*–*V* parameters of the PSC doping by different content of CsI. It is observed that a small amount of CsI addition (≤8%) shows an improvement in V_{OC}, J_{SC}, FF, and PCE of the device, which is attributed to the enlarged grain size, improved crystallinity, and increased absorption ability of $Cs_xFA_{1-x}SnI_3$ film. However, further increasing the content of CsI leads to the decreased performance of PSCs, which may be attributed to the presence of some cracks and pinholes on the film surface when CsI content is high. 8% CsI perovskite film shows the best photovoltaic performance with a V_{OC} of 0.44 V, J_{SC} of 20.70 mA/cm^2, FF of 66.8%, and PCE of 6.08% by forward scan and a V_{OC} of 0.44 V, J_{SC} of 20.48 mA/cm^2, FF of 66.6%, and PCE of 6.00% by reverse scan (Figure 2d). The power output tracking curve in Figure 2d demonstrates the maximum power point (MPP) at ~0.33 V. Figure 2e shows the spectrum of the external quantum efficiency (EQE) of 0% and 8% CsI based devices along with the integrated J_{SC} by calculating the overlap integral between the EQE spectrum and standard AM1.5 solar emission. The integrated J_{SC} value agrees well with the measured results. It is worth noting that the EQE response edge is red-shifted from 900 nm (0% CsI) to 920 nm (8% CsI), which is consistent with the optical characterization of the red-shifted absorption edge and PL emission of $Cs_xFA_{1-x}SnI_3$ films (Figure 1i–k). Figure 2f shows the histograms of PCE for 30 PSCs based on 0% CsI and 8% CsI device from four different batches, demonstrating a higher average performance and better reproducibility of Cs-doped $FASnI_3$ PSCs. To confirm the key role of Cs^+ over I^-, we introduced different Br sources (8% CsBr and 8% FABr) into $FASnI_3$ to compare the device performance, as shown in Figure S6. It can be seen that using the same film fabrication process, CsI- and CsBr-doped devices show improved PCE while the FABr-doped device shows reduced PCE compared to the control device, indicating that Cs plays a key role in determining the photovoltaic properties of the doped perovskite.

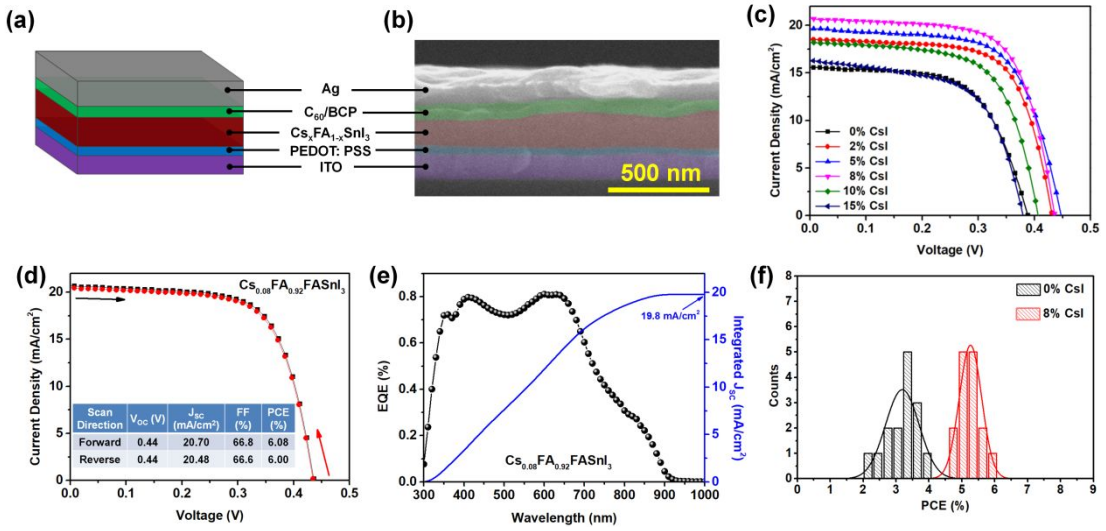

Figure 2. (a) Illustration and (b) cross-sectional SEM image of PSC device structure used in this work. (c) *J*–*V* curves of the FASnI3 PSCs with different CsI content. (d) *J*–*V* and power output tracking curves of the best-performing 8% CsI solar cell measured under reverse and forward voltage scanning. (d) EQE and integrated J_{SC} of the best-performing 8% CsI solar cell. (e) EQE spectra of PSCs based on 0% CsI and 8% CsI films. (f) Histograms of PCEs for 30 solar cell devices of 0% CsI and 8% CsI.

Table 1. Performance parameters of the $Cs_xFA_{1-x}SnI_3$ PSCs with different CsI content

CsI content [%]	V_{OC} [V]	J_{SC} [mA/cm^2]	FF [%]	PCE [%]
0	0.39	15.59	61.3	3.73
2	0.43	18.53	67.9	5.41
5	0.45	19.64	64.9	5.74
8	0.44	20.70	66.7	6.08
10	0.41	18.21	63.8	4.76
15	0.37	16.28	61.4	3.70

To disclose the improved photovoltaic performance of Csdoped $FASnI_3$ film, space charge limited current (SCLC) and electrochemical impedance spectroscopy (EIS) measurements are carried out. The hole-only device is fabricated to reveal the electronic property of the $FASnI_3$ films with or without Cs doping [41]. Figure 3a,b shows the SCLC curves of the PSC device with structure of ITO/PEDOT:PSS/perovskite/PTAA/ Au. It can be seen that hole trap-state density (n_{trap}) shows two-fold reduction after Cs doping (from 6.31×10^{15} cm^{-3} down to 3.31×10^{15} cm^{-3}), implying that the typical defects in $FASnI_3$ structure (i.e., Sn vacancy) can be suppressed after Cs doping. The reduced hole trap state density is further confirmed by XPS measurement. In $FASnI_3$ perovskite, the hole trap state is attributed to the oxidation of Sn^{2+} into Sn^{4+}, so a lower proportion of Sn^{4+} in the perovskite structure indicates a lower trap state density. In Figure 3c, the four peaks deconvoluted from the XPS spectra at ~486.6 (495.1) and 487.2 (495.6) eV are associated with Sn^{2+} and Sn^{4+}, respectively [26]. It can be clearly observed that the proportion of Sn^{4+} in the 8% CsI doped film is significantly reduced compared to that in pure $FASnI_3$, indicating the presence of Cs in the $FASnI_3$ structure prevents the oxidation of Sn^{2+} during film fabrication. It is the consensus that the defect trap states are shown to exist at the grain boundaries (GBs) [41], so the lowered trap state density here is in agreement with the enlarged grain size of Cs-doped $FASnI_3$ film (Figure 1f).

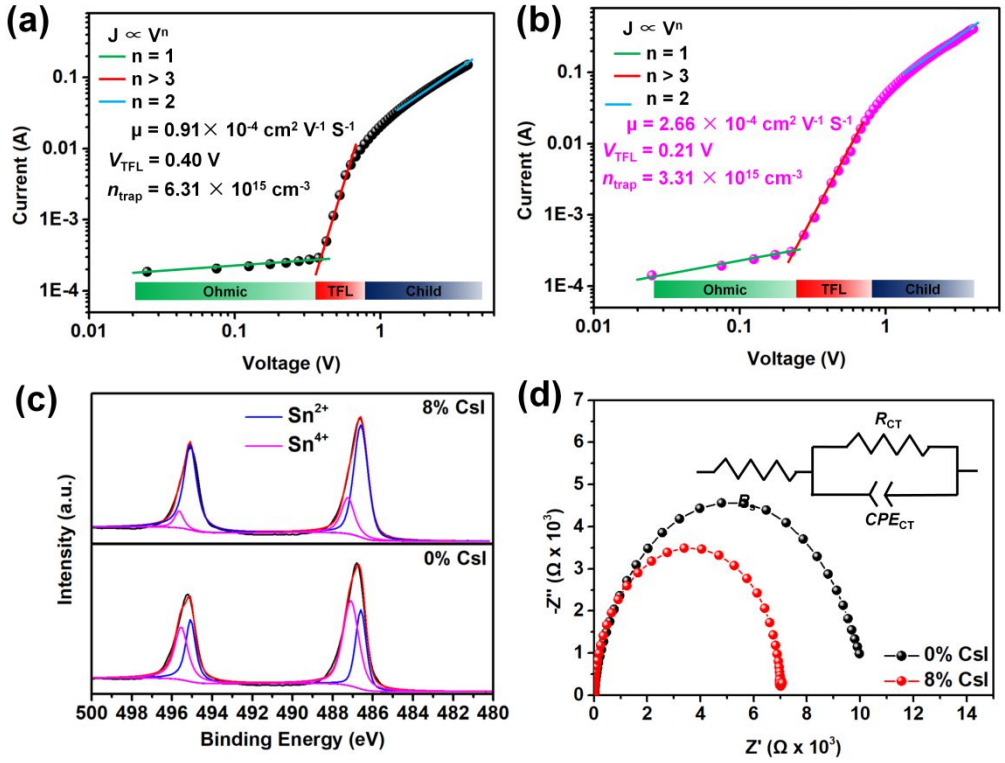

Figure 3. SCLC measurement of (a) 0% and (b) 8% CsI doped device. (c) XPS and (d) EIS characterization of 0% CsI and 8% CsI doped devices.

From SCLC measurements, the carrier mobility after Cs doping (2.66×10^{-4} cm^{2}V^{-1}S^{-1}) is almost three times higher than control device (0.91×10^{-4} cm^{2}V^{-1}S^{-1}), demonstrating the efficient charge transport within the $Cs_xFA_{1-x}SnI_3$ film. EIS is further conducted to confirm the charge transport properties in PSCs (Figure 3d).

The model for fitting EIS results is shown in the inset of Figure 3d, where RS is the sheet resistance and RCT is related to the overall charge-transfer resistance of the device, including the contribution of PEDOT:PSS/perovskite interface, perovskite film, and perovskite/C60 interface. Because the PEDOT:PSS and C60 layer of the device are fabricated under the same process, the RCT is mainly contributed by the charge-transfer resistance of perovskite layer [42−44]. It can be clearly seen that after 8% CsI doping, the arc of the Nyquist plots becomes smaller, indicating the reduced bulk resistance of Cs-doped film. This result is in agreement with the increased charge mobility as shown in Figure 3b. Therefore, the improved charge-transfer ability after Cs doping could efficiently promote the charge collection in the PSCs and lead to the improved performance of PSCs.

We further test the stability of PSC devices with or without Cs doping under different conditions, including in N_2, in air, under illumination, and under annealing. As shown in Figure 4a, the 8% CsI device shows a significantly enhanced stability (maintains ~90% of initial PCE remaining after 2000 h, from 5.53% to 4.94%) when it is stored in N_2, while an obviously decreased PCE is observed in the control device (Figure S8, from 3.85% to 0.43%). To the best of our knowledge, this device stability is the highest value reported to date based on 3D Sn-based PSCs stored in N_2 (Table 2). Note that $MASnI_3$- and $CsSnI_3$-based PSCs show rather poor stability, so they are not discussed here [8]. The air stability of the 8% CsI device is also enhanced compared with the control device (Figures 4b and S9). The PCE of the 0% CsI device drops from 3.18% to 0.13%, while that of the 8% CsI device reduces from 5.49% to 2.79%. Under continuous illumination under AM1.5 conditions at the MPP of the device, 8% CsI device shows more stable steady-state photocurrent than the control one over a period of 800 s (Figure 4c). Figure S10 shows the *J*−*V* and power output tracking curves of the devices used for the steady-state photocurrent measurement. Moreover, the Csdoped device shows robust thermal stability, which remains ~68% of the initial PCE after heating for 220 min at 100°C (Figures 4d and S11). The PCE of 0% CsI device drops from 2.49% to 0.58%, while that of the 8% CsI device reduces from 4.43% to 3.02%. In addition, the UV−vis and XRD measurements of 0% and 8% CsI films before and after heating under 100°C for 60 min (Figure S12) also reveal the good thermal stability after Cs doping. Specifically, no obvious change is observed in the 8% CsI device after annealing, while the 0% CsI device suffers from decreased absorption as well as crystallinity.

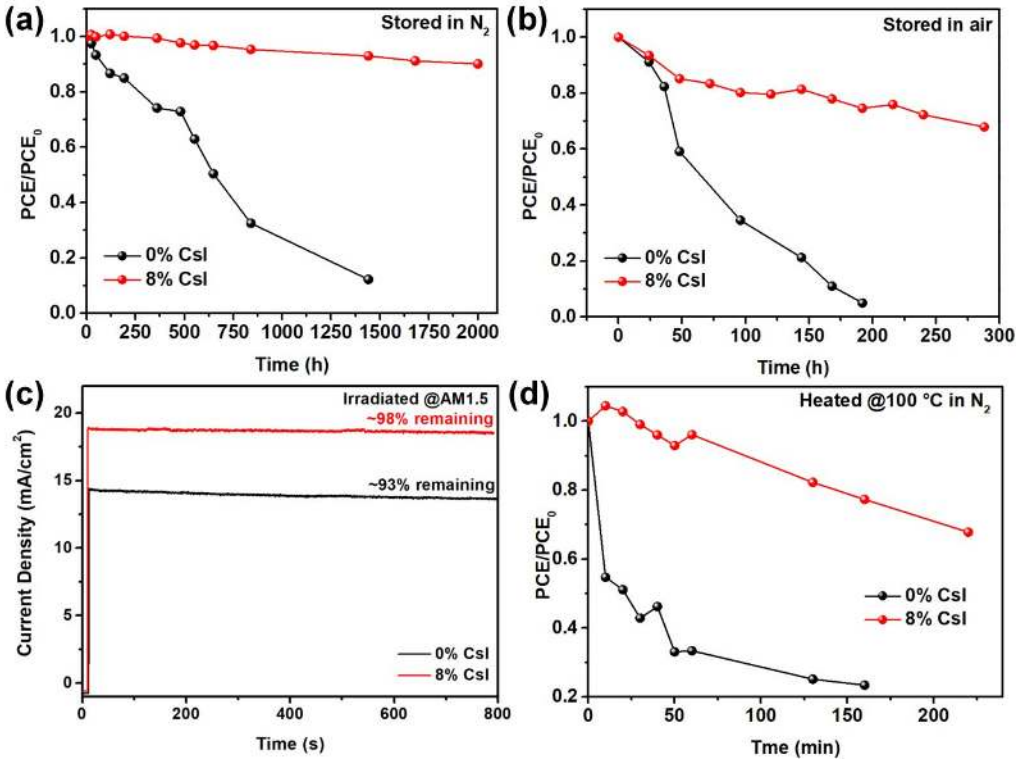

Figure 4. Stability tests of PSC devices with or without Cs doping under different conditions: (a) Stored in N_2, (b) stored in air, (c) illuminated at AM1.5, and (d) heated at 100°C. The stability statistics are based on 6 PSCs in panels a, b, and d.

Table 2. Summary of the device stability test of 3D Sn-based lead-free PSCs stored in N_2 as reported in the literature

Active layer	Device structure	V_{OC} [V]	J_{SC} [mA/cm^2]	FF [%]	PCE [%]	Test period [h]	Remaining PCE	Ref.
$FASnI_3$	Normal	0.47	22.45	67.8	7.09	480	90%	18
$FASnI_3$	Inverted	0.30	7.62	53.0	1.21	70	0%	23
$FASnI_3$	Inverted	0.36	17.60	62.7	4.00	1200	0%	40
$FA_{0.75}MA_{0.25}SnI_3$	Inverted	0.61	21.20	62.7	8.12	400	80%	16
$FA_{0.75}MA_{0.25}SnI_3$	Inverted	0.55	20.0	65.0	7.10	70	100%	41
$Cs_{0.08}FA_{0.92}SnI_3$	**Inverted**	**0.44**	**20.70**	**66.7**	**6.08**	**2000**	**90%**	**This work**

We now aim to explain the improved device stability from the perspectives of structure geometry and thermodynamics. Experimental results (Figure 3a–c) have shown that the hole trap state and Sn^{4+} content are reduced after Cs doping, which could make a solid contribution to the improved stability of the PSCs. In addition to this, crystal structure symmetry is also an important factor that determines the phase stability of the material. As discussed above, the Goldschmidt tolerance factor, t, determines whether a perovskite material with ABX_3 composition forms the cubic phase. In general, materials with t in the range of 0.9−1.0 could form the ideal cubic structure, which is composed of the A cation surrounded by the corner-sharing BX_6 octahedra. When t is in the range of 0.8−0.9 and 1.0−1.1, the BX_6 octahedra will show contraction or distraction tendency; thus, the crystal symmetry is partially reduced [35]. For $FASnI_3$ perovskite material, its t is calculated to be 1.04 (Figure 5a), which indicates the slightly expanded crystal lattice. To achieve t close to 1, it is rational to replace FA^+ by a cation with a smaller ion radius according to the Goldschmidt rule [47]. The doping of $FASnI_3$ with Cs could tune the tolerance factor downward from 1.04 into the high-symmetry cubic phase region (Figure 5a). In this case, the slightly dilatant SnI_6 octahedra in $FASnI_3$ will be contracted and regulated into ordered cubic structure after being doped by appropriate content of Cs, as illustrated in Figure 5b. For a composition of $A'_xA_{1-x}SnI_3$, it can be estimated that $R_A(\text{effective}) = x\,R_{A'} + (1-x)\,R_A$ [47]. Therefore, the t value of $Cs_{0.08}FA_{0.92}SnI_3$ (8% CsI) perovskite is calculated to be 1.02, which is much closer to 1. As a result, the structural symmetry and stability of $FASnI_3$ is able to be improved via Cs doping.

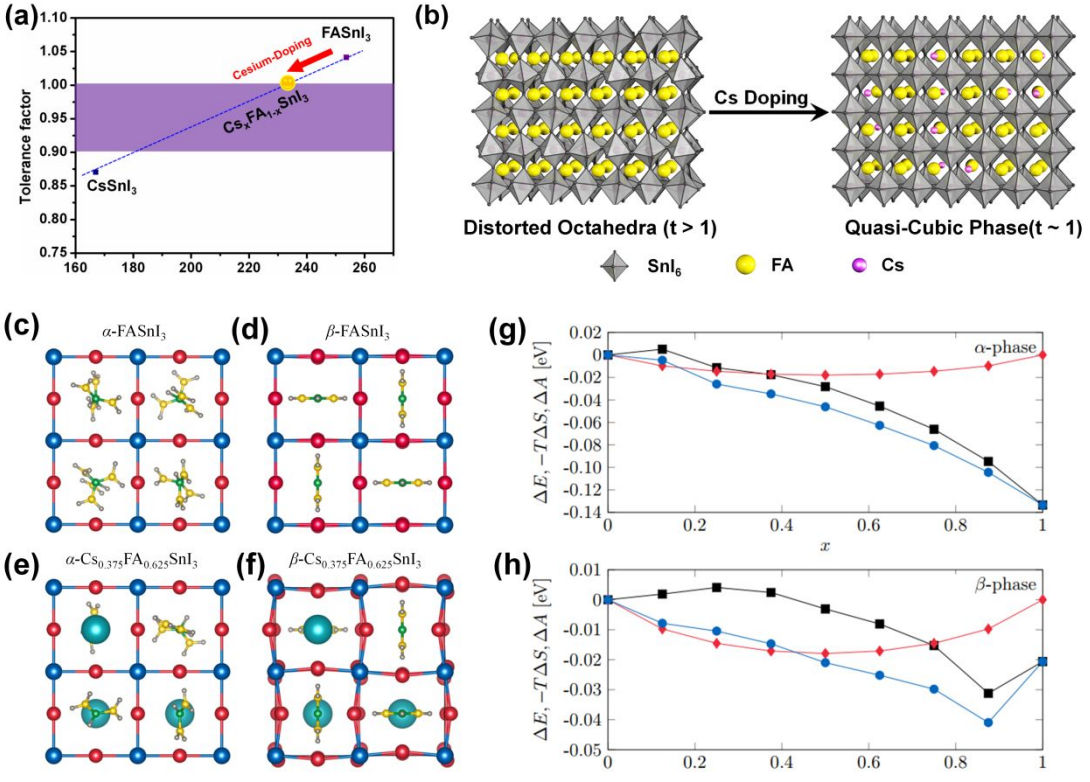

Figure 5. (a) Correlation between the tolerance factor and the effective radius of Cs/FA cation in $Cs_xFA_{1-x}SnI_3$ perovskite. (b) Schematic diagram of the structure transition when $FASnI_3$ is doped by appropriate content of Cs. DFT-optimized structures of different $FASnI_3$ and $Cs_{0.375}FA_{0.625}SnI_3$ structures: (c and e) α-phase and (d and f) β-phase. C, N, H, Cs, Sn, and I atoms are colored in green, yellow, gray, cyan, blue, and red, respectively. Change of internal energy ΔE (black squares), entropy $-T\Delta S$ (red diamonds), and Helmholtz free energy ΔA (blue circles) as a function of x in the perovskite alloy $Cs_xFA_{1-x}SnI_3$ in (g) α-phase and (h) β-phase, where $-T\Delta S$ and ΔA were calculated at $T = 300$ K. All data were shifted so that $\Delta E = 0$ at $x = 0$.

The improved stability of $FASnI_3$ after Cs doping is further explained from the point view of thermodynamics, where first-principles (density functional theory, DFT) theoretical calculation is carried out to investigate the variation of Helmholtz free-energy formation energy in the $Cs_xFA_{1-x}SnI_3$ system. Here, we consider both the α-phase and β-phase of $FASnI_3$, though only α-phase $FASnI_3$ is found to be stable at room temperature [14]. To model the disordered structures of the cubic α-phase, we adopted the 2×2×2 supercell model that host quasi-randomly distributed 8 FA^+ cations in single cells (Figure 5c). For the β-phase, we adopted the 2×2×2 supercell model of a tetragonal lattice with regularly aligned 8 FA^+ cations (Figure 5d). We modeled the Cs-doped $FASnI_3$ by replacing different amounts of FA^+ by Cs^+ in the supercell models. For example, a supercell consisting of 5 FA^+ and 3 Cs^+ corresponds to $x = 0.375$, i.e., $Cs_{0.375}FA_{0.625}SnI_3$ (relaxed samples of different phases are depicted in Figure 5e,f). DFT results of lattice constants indicate that in the α-phase, the unit-cell volume decreases with an increasing doped-Cs amount, and the lattice remains cubic within the whole x range (a = 12.680 and 12.234 Å for x = 0 and 1, respectively). In β-FASnI3, doping Cs also results in contraction of unit-cell volume, and the lattice constants vary within the tetragonal system from $a = b$ = 12.535 Å, c = 12.302 Å for x = 0 to $a = b$ = 12.055 Å, c = 12.398 Å for x = 1. Figure 5g,h shows the change of internal energy ΔE (calculated with DFT), entropy of mixing $-T\Delta S = -k_BT$ [$x \log(x) + (1-x) \log(1-x)$] ($T = 300$ K), and Helmholtz free energy $\Delta A = \Delta E - T\Delta S$ as functions of x in the α- and β-phases of $Cs_xFA_{1-x}SnI_3$. It can be observed that with the increase of Cs, the internal energy and free energy of α-$FASnI_3$ perovskite gradually decrease, indicating the enhanced thermodynamic stability of $Cs_xFA_{1-x}SnI_3$ structure at room temperature.

In summary, we have developed a structural regulation strategy to modify the structure of $FASnI_3$ perovskite. We have theoretically and experimentally demonstrated that the inserting of small-radius Cs into the crystal lattice of $FASnI_3$ perovskite leads to the contraction of $FASnI_3$ crystal structure and lowered free energy, leading to reduced trap state density, improved symmetry, and enhanced thermodynamic stability. As a result, the PSC devices based on Cs-doped $FASnI_3$ film show remarkable device stability (loss of only 10% of its initial PCE after 2000 h of storage in N_2). More importantly, the device also exhibits enhanced stability under illumination, heating, or exposure in air. Moreover, the best performing PSC device after Cs doping shows a 63% increase in PCE compared to the control device (from 3.74% to 6.08%) with negligible hysteresis, which is confirmed to originate from the lowered trap state density and improved charge mobility of Cs-doped $FASnI_3$. This work could provide an important practical strategy for further boosting the performance (both PCE and stability) of the PSCs based on $FASnI_3$ material.

Acknowledgements
This work was financially supported by National Natural Science Foundation of China (Grant Nos. 11574248 and 61875161), China Postdoctoral Science Foundation (Grant No. 2016M590947), the Fundamental Research Funds for the Central Universities (Grant No. xjj2016031), the National Natural Science Foundation of China (Grant No. 61505161), the Natural Science Basic Research Plan of Shaanxi Province (Grant No. 2017JM6064), and the Scientific Research Plan Projects of Shaanxi Education Department (Grant No. 17JK0700). The SEM and TEM work was done at International Center for Dielectric Research (ICDR), Xi'an Jiaotong University, Xi'an, China. J.L. thanks the generous allocation of computing resources by the CSC − IT Center for Science and the Aalto Science−IT project. The SEM work was performed at the International Center of Dielectric Research (ICDR), Xi'an Jiaotong University, Xi'an, China. The authors also thank Ma and Dai for their help in using SEM equipment.

Reference

1. Pan, W.; Wu, H.; Luo, J.; Deng, Z.; Ge, C.; Chen, C.; Jiang, X.; Yin, W.; Niu, G.; Zhu, L.; et al. $Cs_2AgBiBr_6$ Single-Crystal X-Ray Detectors with A Low Detection Limit. *Nat. Photonics* **2017**, 11, 726−732.
2. Dai, J.; Xi, J.; Li, L.; Zhao, J.; Shi, Y.; Zhang, W.; Ran, C.; Jiao, B.; Hou, X.; et al. Functional Conjugated Ligands Assisted Charge Transport between Coupling Colloidal Perovskite Quantum Dots. *Angew. Chem., Int. Ed.* **2018**, 57, 5754−5785.
3. Shi, Y.; Wu, W.; Dong, H.; Li, G.; Xi, K.; Divitini, G.; Ran, C.; Yuan, F.; Zhang, M.; Jiao, B.; et al. A Strategy for Architecture Design of Crystalline Perovskite Light-Emitting Diodes with High Performance. *Adv. Mater.* **2018**, 30, 1800251.
4. Grätzel, M. The Light and Shade of Perovskite Solar Cells. *Nat. Mater.* **2014**, *13*, 838−842.
5. Babayigit, A.; Ethirajan, A.; Muller, M.; Conings, B. Toxicity of Organometal Halide Perovskite Solar Cells. *Nat. Mater.* **2016**, *15*, 247−251.
6. Jeon, N. J.; H. Na,; Jung, E. H.; Yang, T. Y.; Lee, Y. G.; Kim, G.; Shin, H. W.; Seok, S. I.; Lee, J.; Seo, J. A Fluorene-Terminated Hole-Transporting Material for Highly Efficient and Stable Perovskite Solar Cells. *Nat. Energy* **2018**, *3*, 682−689.
7. Shi, Z. J.; Guo, J.; Chen, Y. H.; Li, Q.; Pan, Y. F.; Zhang, H. J.; Xia, Y. D.; Huang, W. Lead-Free Organic-Inorganic Hybrid Perovskites for Photovoltaic Applications: Recent Advances and Perspectives. *Adv. Mater.* **2017**, *29*, 1605005.
8. Konstantakou, M.; Stergiopoulos, T. A Critical Review on Tin Halide Perovskite Solar Cells. *J. Mater. Chem. A* **2017**, *5*, 11518−11549.
9. Krishnamoorthy, T.; Ding, H.; Yan, C.; Leong, W. L.; Baikie, T.; Zhang, Z. Y.; Sherburne, M.; Li, S.; Asta, M.; Mathews, N.; Mhaisalkar, S. G. Lead-Free Germanium Iodide Perovskite Materials for Photovoltaic Applications. *J. Mater. Chem. A* **2015**, *3*, 23829−23832.
10. Park, B. W.; Philippe, B.; Zhang, X. L.; Rensmo, H.; Boschloo, G.; Johansson, E. M. J. Bismuth Based Hybrid Perovskites $A_3Bi_2I_9$ (A: Methylammonium or Cesium) for Solar Cell Application. *Adv. Mater.* **2015**, *27*, 6806−6813.
11. Ran, C.; Wu, Z.; Xi, J.; Yuan, F.; Dong, H.; Lei, T.; He, X.; Hou, X. Construction of Compact Methylammonium Bismuth Iodide Film Promoting Lead-Free Inverted Planar Heterojunction Organohalide Solar Cells with Open-Circuit Voltage over 0.8 V. *J. Phys. Chem. Lett.* **2017**, *8*, 394−400.
12. Singh, A.; Boopathi, K. M.; Mohapatra, A.; Chen, Y. F.; Li, G.; Chu, C. W. Photovoltaic Performance of Vapor-Assisted Solution-Processed Layer Polymorph of $Cs_3Sb_2I_9$. *ACS Appl. Mater. & Interfaces* **2018**, *10*, 2566−2573.
13. Cortecchia, D.; Dewi, H. A.; Yin, J.; Bruno, A.; Chen, S.; Baikie, T.; Boix, P. P.; Grätzel, M.; Mhaisalkar, S.; Soci, C.; Mathews, N. Lead-Free $MA_2CuCl_xBr_{4-x}$ Hybrid Perovskites. *Inorg. Chem.* **2016**, *55*, 1044−1052.
14. Stoumpos, C. C.; Malliakas, C. D.; Kanatzidis, M. G. Semiconducting Tin and Lead Iodide Perovskites with Organic Cations: Phase Transitions, High Mobilities, and Near-Infrared Photoluminescent Properties. *Inorg. Chem.* **2013**, *52*, 9019−9038.
15. Koh, T. M.; Krishnamoorthy, T.; Yantara, N.; Shi, C.; Leong, W. L.; Boix, P. P.; Grimsdale, A. C.; Mhaisalkar, S. G.; Mathews, N. Formamidinium Tin-Based Perovskite with Low E_g for Photovoltaic Applications. *J. Mater. Chem. A* **2015**, *3*, 14996−15000.
16. Lee, S. J.; Shin, S. S.; Kim, Y. C.; Kim, D.; Ahn, T. K.; Noh, J. H.; Seo, J.; Seok, S. I. Fabrication of Efficient Formamidinium Tin Iodide Perovskite Solar Cells through SnF_2–Pyrazine Complex. *J. Am. Chem. Soc.* **2016**, *138*, 3974−3977.
17. Ke, W. J.; Stoumpos, C. C.; Logsdon, J. L.; Wasielewski, M. R.; Yan, Y. F.; Fang, G. J.; Kanatzidis, M. G. TiO_2–ZnS Cascade Electron Transport Layer for Efficient Formamidinium Tin Iodide Perovskite Solar Cells. *J. Am. Chem. Soc.* **2016**, *138*, 14998−15003.
18. Liao, W. Q.; Zhao, D. W.; Yu, Y.; Grice, C. R.; Wang, C. L.; Cimaroli, A. J.; Schulz, P.; Meng, W. W.; Zhu, K.; Xiong, R. G.; Yan, Y. F. Lead-Free Inverted Planar Formamidinium Tin Triiodide Perovskite Solar Cells Achieving Power Conversion Efficiencies up to 6.22%. *Adv. Mater.* **2016**, *28*, 9333−9340.

19. Zhao, Z. R.; Gu, F. D.; Li, Y. L.; Sun, W. H.; Ye, S. Y.; Rao, H. X.; Liu, Z. W.; Bian, Z. Q.; Huang, C. H. Mixed-Organic-Cation Tin Iodide for Lead-Free Perovskite Solar Cells with an Efficiency of 8.12%. *Adv. Sci.* **2017**, *4*, 1700204.
20. Shao, S. Y.; Liu, J.; Portale, G.; Fang, H. H.; Blake, G. R.; ten Brink, G. H.; Koster, L. J. A.; Loi, M. A. Highly Reproducible Sn-Based Hybrid Perovskite Solar Cells with 9% Efficiency. *Adv. Energy Mater.* **2018**, *8*, 1702019.
21. Zhu, Z. L.; Chueh, C. C.; Li, N.; Mao, C. Y.; Jen, A. K. Y. Realizing Efficient Lead-Free Formamidinium Tin Triiodide Perovskite Solar Cells *via* a Sequential Deposition Route. *Adv. Mater.* **2018**, *30*, 1703800.
22. Ke, W. J.; Stoumpos, C. C.; Zhu, M. H.; Mao, L. L.; Spanopoulos, I.; Liu, J.; Kontsevoi, O. Y.; Chen, M.; Sarma, D.; Zhang, Y. B.; Wasielewski, M. R.; Kanatzidis, M. G. Enhanced Photovoltaic Performance and Stability with a New Type of Hollow 3D Perovskite {en}$FASnI_3$. *Sci. Adv*. **2017**, *3*, e1701293.
23. Xi, J.; Wu, Z. X.; Jiao, B.; Dong, H.; Ran, C.; Piao, C. C.; Lei, T.; Song, T. B.; Ke, W. J.; Yokoyama, T.; Hou, X.; Kanatzidis, M. G. Multichannel Interdiffusion Driven $FASnI_3$ Film Formation Using Aqueous Hybrid Salt/Polymer Solutions toward Flexible Lead-Free Perovskite Solar Cells. *Adv. Mater.* **2017**, *29*, 1606964.
24. Chen, K.; Wu, P.; Yang, W. Q.; Su, R.; Luo, D. Y.; Yang, X. Y.; Tu, Y. G.; Zhu, R.; Gong, Q. H. Low-Dimensional Perovskite Interlayer for Highly Efficient Lead-Free Formamidinium Tin Iodide Perovskite Solar Cells. *Nano Energy* **2018**, *49*, 411−418.
25. Lee, S. J.; Shin, S. S.; Im, J.; Ahn, T. K.; Noh, J. H.; Jeon, N. J.; Seok, S. I.; Seo, J. Reducing Carrier Density in Formamidinium Tin Perovskites and Its Beneficial Effects on Stability and Efficiency of Perovskite Solar Cells. *ACS Energy Lett.* ***2018***, ***3***, 46−53.
26. Liao, Y. Q.; Liu, H. F.; Zhou, W. J.; Yang, D. W.; Shang, Y. Q.; Shi, Z. F.; Li, B. H.; Jiang, X. Y.; Zhang, L. J.; Quan, L. N.; Quintero-Bermudez, R.; Sutherland, B. R.; Mi, Q. X.; Sargent, E. H.; Ning, Z. L. Highly Oriented Low-Dimensional Tin Halide Perovskites with Enhanced Stability and Photovoltaic Performance. *J. Am. Chem. Soc.* **2017**, *139*, 6693−6699.
27. Ran, C.; Xi, J.; Gao, W.; Yuan, F.; Lei, T.; Jiao, B.; Hou, X.; Wu, Z. Bilateral Interface Engineering toward Efficient 2D–3D Bulk Heterojunction Tin Halide Lead-Free Perovskite Solar Cells. *ACS Energy Lett.* **2018**, *3*, 713−721.
28. Wang, F.; Ma, J. L.; Xie, F. Y.; Li, L. K.; Chen, J.; Fan, J.; Zhao, N. Organic Cation-Dependent Degradation Mechanism of Organotin Halide Perovskites. *Adv. Funct. Mater.* **2016**, *26*, 3417−3423.
29. Liu, X. L.; Feng, Y.; Cui, H. T.; Liu, F. Y.; Hao, X. J.; Conibeer, G.; Mitzi, D. B.; Green, M. The Current Status and Future Prospects of Kesterite Solar Cells: a Brief Review. *Prog. Photovoltaics* **2016**, *24*, 879−898.
30. Marshall, K. P.; Walker, M.; Walton, R. I.; Hatton, R. A. Enhanced Stability and Effciency in Hole-Transport-Layer-Free $CsSnI_3$ Perovskite Photovoltaics. *Nat. Energy* **2016**, *1*, 16178.
31. Marshall, K. P.; Walton, R. I.; Hatton, R. A. Tin Perovskite/Fullerene Planar Layer Photovoltaics: Improving the Efficiency and Stability of Lead-Free Devices. *J. Mater. Chem. A* **2015**, *3*, 11631−11640.
32. Kontos, A. G.; Kaltzoglou, A.; Siranidi, E.; Palles, D.; Angeli, G. K.; Arfanis, M. K.; Psycharis, V.; Raptis, Y. S.; Kamitsos, E. I.; Trikalitis, P. N.; Stoumpos, C. C.; Kanatzidis, M. G.; Falaras, P. Structural Stability, Vibrational Properties, and Photoluminescence in CsSnI3 Perovskite upon the Addition of SnF_2. *Inorg. Chem*. **2017**, *56*, 84−91.
33. Li, W. Z.; Li, J. W.; Li, J. L.; Fan, J. D.; Mai, Y. H.; Wang, L. D. Addictive-Assisted Construction of All-Inorganic $CsSnIBr_2$ Mesoscopic Perovskite Solar Cells with Superior Thermal Stability up to 473 K. *J. Mater. Chem. A* **2016**, *4*, 17104−17110.
34. Song, T. B.; Yokoyama, T.; Stoumpos, C. C.; Logsdon, J.; Cao, D. H.; Wasielewski, M. R.; Aramaki, S.; Kanatzidis, M. G. Importance of Reducing Vapor Atmosphere in the Fabrication of Tin-Based Perovskite Solar Cells. *J. Am. Chem. Soc.* **2017**, *139*, 836−842.
35. Zhao, Y. X.; Zhu, K. Organic-Inorganic Hybrid Lead Halide Perovskites for Optoelectronic and Electronic Applications. *Chem. Soc. Rev.*, **2016**, *45*, 655−689.
36. Xiao, Z. W.; Lei, H. C.; Zhang, X.; Zhou, Y. Y.; Hosono, H.; Kamiya, T. Ligand-Hole in $[SnI_6]$ Unit and Origin of Band Gap in Photovoltaic Perovskite Variant Cs_2SnI_6. *B. Chem. Soc. Jpn.* **2015**, *88*,

1250−1255.
37. Saliba, M.; Matsui, T.; Domanski, K.; Seo, J. Y.; Ummadisingu, A.; Zakeeruddin, S. M.; Correa-Baena, J. P.; Tress, W. R.; Abate, A.; Hagfeldt, A.; Grätzel, M. Incorporation of Rubidium Cations into Perovskite Solar Cells Improves Photovoltaic Performance. *Science* **2016**, *354*, 206−209.
38. Park, N. G. Perovskite Solar Cells: an Emerging Photovoltaic Technology. *Mater. Today* **2015**, *18*, 65−72.
39. Gao, W.; Ran, C.; Xi, J.; Jiao, B.; Zhang, W.; Wu, M.; Hou, X.; Wu, Z. High-Quality $Cs_2AgBiBr_6$ Double Perovskite Film for Lead-Free Inverted Planar Heterojunction Solar Cells with 2.2 % Efficiency. *ChemPhysChem* **2018**, *19*, 1696−1700.
40. Prasanna, R.; Gold-Parker, A.; Leijtens, T.; Conings, B.; Babayigit, A.; Boyen, H. G.; Toney, M. F.; McGehee, M. D. Band Gap Tuning *via* Lattice Contraction and Octahedral Tilting in Perovskite Materials for Photovoltaics. *J. Am. Chem. Soc.* **2017**, *139*, 11117−11124.
41. Ran, C.; Xu, J.; Gao, W.; Huang, C.; Dou, S. Defects in Metal Triiodide Perovskite Materials towards High-Performance Solar Cells: Origin, Impact, Characterization, and Engineering. *Chem. Soc. Rev.*, **2018**, *47*, 4581−4610.
42. Yang, Y. Y.; Xiao, J. Y.; Wei, H. Y.; Zhu, L. F.; Li, D. M.; Luo, Y. H.; Wu, H. J.; Meng, Q. B. An All-Carbon Counter Electrode for Highly Efficient Hole-Conductor-Free Organo-Metal Perovskite Solar Cells. *RSC Adv.* **2014**, *4*, 52825−52830.
43. Chen, C.; Liu, D.; Zhang, B.; Bi, W.; Li, H.; Jin, J.; Chen, X.; Xu, L.; Song, H.; Dai, Q. Carrier Interfacial Engineering by Bismuth Modifcation for Effcient and Thermoresistant Perovskite Solar Cells. *Adv. Energy Mater.* **2018**, 8, 1703659.
44. Chen, C.; Li, H.; Jin, J.; Cheng, Y.; Liu, D.; Song, H.; Dai, Q. Highly Enhanced Long Time Stability of Perovskite Solar Cells by Involving a Hydrophobic Hole Modification Layer. *Nano Energy* **2017**, 32, 165−173.
45. Jokar, E.; Chien, C.; Fathi, H. A.; Rameez, M.; Chang, Y. H.; Diau, E. W. G. Slow Surface Passivation and Crystal Relaxation with Additives to Improve Device Performance and Durability for Tin-Based Perovskite Solar Cells. *Energy Environ. Sci.* **2018**, *11*, 2353−2362.
46. Liu, J.; Ozaki, M.; Yakumaru, S.; Handa, T.; Nishikubo, R.; Kanemitsu, Y.; Saeki, A.; Murata, Y.; Murdey, R.; Wakamiya, A. Lead-Free Solar Cells based on Tin Halide Perovskite Films with High Coverage and Improved Aggregation *Angew. Chem. Int. Ed.*, 2018, **57**, 13221−13225.
47. Li, Z.; Yang, M. J.; Park, J. S.; Wei, S. H.; Berry, J. J.; Zhu, K. Stabilizing Perovskite Structures by Tuning Tolerance Factor: Formation of Formamidinium and Cesium Lead Iodide Solid-State Alloys. *Chem. Mater.* **2016**, *28*, 284−292.